American Mineralogist, Volume 92, pages 1148–1157, 2007

Thermal infrared spectroscopy and modeling of experimentally shocked basalts

JEFFREY R. JOHNSON,[1,*] MATTHEW I. STAID,[2] AND MICHAEL D. KRAFT[3]

[1]United States Geological Survey, 2255 N. Gemini Drive, Flagstaff, Arizona 86001, U.S.A.
[2]Planetary Science Institute, Tucson, Arizona 85719, U.S.A.
[3]Arizona State University, Tempe, Arizona 85287, U.S.A.

ABSTRACT

New measurements of thermal infrared emission spectra (250–1400 cm^{-1}; ~7–40 μm) of experimentally shocked basalt and basaltic andesite (17–56 GPa) exhibit changes in spectral features with increasing pressure consistent with changes in the structure of plagioclase feldspars. Major spectral absorptions in unshocked rocks between 350–700 cm^{-1} (due to Si-O-Si octahedral bending vibrations) and between 1000–1250 cm^{-1} (due to Si-O antisymmetric stretch motions of the silica tetrahedra) transform at pressures >20–25 GPa to two broad spectral features centered near 950–1050 and 400–450 cm^{-1}. Linear deconvolution models using spectral libraries composed of common mineral and glass spectra replicate the spectra of shocked basalt relatively well up to shock pressures of 20–25 GPa, above which model errors increase substantially, coincident with the onset of diaplectic glass formation in plagioclase. Inclusion of shocked feldspar spectra in the libraries improves fits for more highly shocked basalt. However, deconvolution models of the basaltic andesite select shocked feldspar end-members even for unshocked samples, likely caused by the higher primary glass content in the basaltic andesite sample.

Keywords: Shock, infrared, spectroscopy, basalt, deconvolution, Mars

INTRODUCTION

The surfaces of the terrestrial planets have been altered extensively by impact cratering throughout their evolution at scales ranging from mineral boundaries to impact basins. At the smallest scales, minerals experience structural disorder to varying degrees when subjected to high shock pressures from impacts. Such deviations in crystal lattices can be documented with thermal infrared spectroscopy owing to the sensitivity of this technique to vibrational motions in crystal structures. For example, thermal infrared analyses of experimentally and naturally shocked minerals and rocks reveal degradation in the spectral detail and position of absorption features with increasing shock pressure. This is attributable to lattice disordering and increasing glass content, particularly at shock pressures above ~20 GPa for plagioclase feldspars (Lyon 1963; Bunch et al. 1967, 1968; Stöffler 1971, 1972, 1974; Stöffler and Hornemann 1972; Arndt et al. 1982; Ostertag 1983). These types of spectral effects also have been observed in thermal infrared laboratory studies of meteorites (e.g., Cooney et al. 1999; Xie et al. 2001; Wright et al. 2006; Palomba et al. 2006). Although remotely sensed thermal infrared observations of planetary surfaces provide important constraints on surface mineralogy and/or physical properties (e.g., Christensen et al. 1998, 2001; Sprague et al. 2002; Salisbury et al. 1995, 1997; Morris et al. 1999; Ramsey 2002), few studies have investigated the spectral effects of high shock pressures in detail (cf. Wright et al. 2004; Johnson et al. 2006).

Because pyroxene and olivine crystal lattices are relatively resistant to shock pressure compared to feldspars, changes in the structure and thermal infrared spectral features of feldspars provide the best means to study shock effects in basaltic rocks (cf. Johnson et al. 2002). Slight disordering in the feldspar structure begins at pressures >15–20 GPa. Diaplectic glass (maskelynite) formation is complete between ~30–45 GPa and significant melting occurs greater than ~45 GPa (Stöffler 1972; Gibbons et al. 1975; Hörz and Cintala 1997; Velde et al. 1987, 1989), depending on the absolute strain rate, shock-pulse duration, and initial temperature (Stöffler 2001; DeCarli et al. 2002; Fritz et al. 2002). As pressures increase, the mutual existence of crystalline phases and diaplectic glasses cause the characteristic, fourfold (tetrahedral), strong coordination bonds of Si and Al in feldspars to alter to weaker, less polymerized bonds that approach sixfold (octahedral) coordination. This change influences the characteristic vibrational frequencies in the thermal infrared. For example, the bands near 400–550 cm^{-1} are caused by bending vibrations in the Si-O-Al planar ring structures in tectosilicates and diaplectic glasses. Si-O-Si octahedral-bending vibrations cause several weaker absorptions between about 450–700 cm^{-1}, and SiO_6 octahedral-stretching vibrations occur between 750–850 cm^{-1}. Absorptions in the 900–1200 cm^{-1} region are due to Si-O antisymmetric stretch motions of the silica tetrahedral units and Al-O vibrations in the structure (Bunch et al. 1967; Iiishi et al. 1971; Stöffler and Hornemann 1972; Arndt et al. 1982; Ostertag 1983; Velde et al. 1987; Williams and Jeanloz 1988, 1989; Heymann and Hörz 1990; Daniel et al. 1995, 1997; Williams 1998; Yamaguchi and Sekine 2000; King et al. 2004).

* E-mail: jrjohnson@usgs.gov

0003-004X/07/0007–1148$05.00/DOI: 10.2138/am.2007.2356

Johnson et al. (2002, 2003) acquired thermal infrared spectra (250–1400 cm^{-1}) of experimentally shocked nearly monomineralic anorthosite (bytownite, An_{79}) and albitite (An_{02}) samples over peak pressures from 17 to 56 GPa. They documented changes in the appearance and position of spectral features with increasing pressure due to depolymerization of the silica tetrahedra. Unshocked anorthosite samples exhibited strong absorption bands at 1115 cm^{-1} and near 940 cm^{-1}, and weak bands in the 500–650 cm^{-1} region. Unshocked albitite spectral features were sharper and shifted to higher wavenumbers in the 800–1200 cm^{-1} region. At the highest shock pressures, both types of feldspars lost all but two major spectral features, a deep band near 440–460 cm^{-1} (caused by bending vibrations in the Si-O-Al planar ring structures) and broad Si-O stretch bands at 960 cm^{-1} (anorthosite) and 1035 cm^{-1} (albitite).

Here we expand on previous studies of shocked feldspars by presenting thermal infrared emission spectra of experimentally shocked basalt and basaltic andesite (17–63 GPa). These two rock types represent a relevant range of lithologies known or postulated to exist on the surfaces of the terrestrial planets. To investigate the degree to which combinations of other minerals and glasses can replicate the spectra of shocked rocks, we used combinatorial spectral deconvolution techniques incorporating spectral libraries composed of standard mineral end-members with and without supplementary spectra of shocked bytownite and albite feldspars. By expanding the study of shock effects in thermal infrared wavelengths from minerals to igneous rocks, we provide data useful in analyzing remote sensing observations of rocky planetary surface materials.

Methods

Samples

We selected samples of basalt and basaltic andesite, both of which are fine-grained, minimally altered rocks with few phenocrysts. Samples with randomly oriented, millimeter-sized crystals minimized the possible bias of crystal-lattice orientation on the degree and type of shock deformation from the propagating shock wave. Rocks with minimal primary glass content were selected to better observe the loss of crystalline structure (glass formation) with increasing shock pressure. A fine-grained basalt with little glass was selected from the base of the Grand Falls (Arizona) lava flow, and a basaltic andesite with higher glass content was selected from the west side of the SP Flow (Arizona) cone (Ulrich 1987), representing pieces of lava that capped the cone rim.

Quantitative mineral abundances for each sample were calculated from scanning electron microscope (SEM) back-scattered electron (BSE) images of polished thin sections (Fig. 1) and chemical maps (Al, Si, P, Na, Mg, K, Ca, Fe, Ti, and O) produced using energy dispersive spectroscopy (EDS). Each element was mapped to a separate 512 × 512 pixel image file, where the 8-bit value of each pixel represented the relative abundance of that element. A supervised classification was then performed on each image set using a maximum likelihood classification. Regions of interest (ROIs) were selected for each mineral class on the basis of relative elemental abundances. A subsequent low-pass filtering algorithm was run to reduce noise in the classification maps by reclassifying spurious pixels to match the major class of pixels within a 3 × 3 pixel kernel. Post-classification statistical analyses of the mineral maps provided the areal abundance of each mineral class per scene. The results from multiple mineral maps from each sample were averaged to acquire final mineral abundances.

Shock recovery experiments

The Flat Plate Accelerator at the Johnson Space Center, Houston was used to conduct the shock experiments. As detailed by Johnson et al. (2002), a powder propellant gun launches flat metal plates for the production of planar shock waves in targets (cf. Gibbons et al. 1975; Thoma et al. 2005). The geologic target was a disk cored from the rock sample, 12 mm in diameter and 1 mm thick. The disk was encapsulated into a metal holder and placed into a vacuum chamber where it was impacted by a metal flyer plate of some measured velocity. Table 1 lists the details of each experiment for both rock types, including the measured velocity, the metal composition of the flyer plate, and that of the target assembly container. Following an experiment, excess metal from the holder was removed using a lathe until the silicate target could be pried from its original target well. Careful prying allowed for the recovery of relatively large chips (2–10 mm) that were washed with water to remove any clinging fines and dried. Use of the 25 mm barrel allowed for recovery of up to 400 mg. Unshocked samples included both chips broken from the parent rock and the sample blocks from which the thin sections were made.

Thermal infrared spectroscopy

The Nicolet Nexus 670 spectrometer at Arizona State University (ASU) was used to acquire emission spectra (250–1400 cm^{-1}) of the samples. This instrument is equipped with an uncooled, deuterated triglycine sulfate (DTGS) detector and is adapted for emission spectroscopy (Ruff et al. 1997). The spectrometer and samples were placed in a chamber continuously "scrubbed" to remove particulates, CO_2, and water vapor. Energy from a heated particulate sample (maintained at 80 °C) was collected by a parabolic mirror and directed toward the interferometer, and blackbodies at 70 and 100 °C were used for radiometric calibration. The infrared beam was confined to the sample by adjusting the sample location within the optical path. The spectrometer was configured to provide 4 cm^{-1} resolution with 270 scans co-added per spectrum.

Table 1A. Detailed conditions for the Grand Falls basaltic rock shock recovery experiments

EIL no.*†	Impact velocity (km/s)	Flyer plate‡	Assembly‡	Peak pressure (GPa)
3377	1.370	Al2024	SS304	17.4
3378	1.121	SS304	SS304	24.0
3442	1.228	SS304	SS304	26.7
3379	1.322	SS304	SS304	29.0
3380	1.381	SS304	SS304	30.4
3381	1.184	FS77	SS304	33.5
3390	1.406	SS304	FS77	40.9
3383	1.181	FS77	FS77	46.4
3382	1.299	FS77	FS77	52.3
3485	1.272	FS77	FS77	56.2
3483	1.299	FS77	FS77	57.3
3469	1.372	Tungsten	FS77	59.8
3465	1.391	Tungsten	FS77	60.6

* EIL no. [Running Flat Plate Accelerator experiment number in Experimental Impact Laboratory (EIL) at Johnson Space Center].
† Samples 3483 and 3485 were physically combined (average pressure 56.75 GPa), as were samples 3465 and 3469 (average pressure 60.2 GPa).
‡ Projectile and assembly materials (Equation of State): Al2024 = Aluminum 2024 (Marsh 1980), SS304 = Stainless Steel 304 (Marsh 1980), FS77 = Fansteel 77 (a W-Ni alloy; Jones et al. 1966).

Table 1B. Detailed conditions for the SP Flow basaltic rock shock recovery experiments

EIL no.*†	Impact velocity (km/s)	Flyer plate‡	Assembly‡	Peak pressure (GPa)
3455	1.357	Al2024	SS304	17.2
3456	1.114	SS304	SS304	23.9
3457	1.304	SS304	SS304	28.4
3458	1.377	SS304	SS304	30.3
3463	1.232	SS304	FS77	35.0
3459	1.349	FS77	SS304	38.9
3462	1.173	FS77	FS77	43.8
3460	1.294	FS77	FS77	52.2
3482	1.296	FS77	FS77	57.2
3481	1.307	FS77	FS77	57.8
3470	1.420	Tungsten	FS77	62.0
3472	1.439	Tungsten	FS77	63.0

* EIL no. [Running Flat Plate Accelerator experiment number in Experimental Impact Laboratory (EIL) at Johnson Space Center].
† Samples 3481 and 3482 were physically combined (average pressure 57.5 GPa), as were samples 3470 and 3472 (average pressure 62.5 GPa).
‡ Projectile and assembly materials (Equation of State): Al2024 = Aluminum 2024 (Marsh 1980), SS304 = Stainless Steel 304 (Marsh 1980), FS77 = Fansteel 77 (a W-Ni alloy; Jones et al. 1966).

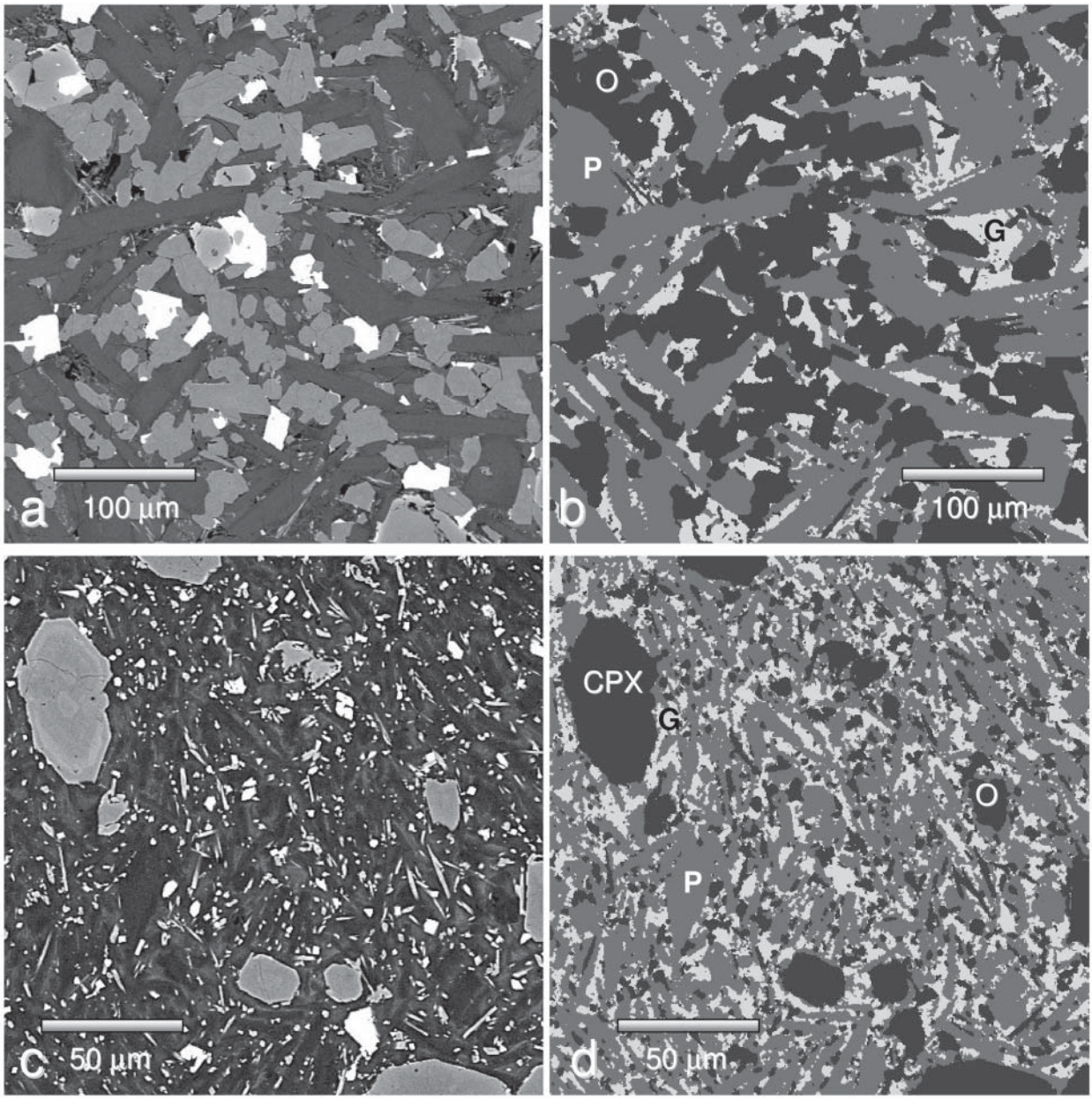

Figure 1. (**a**) BSE images of Grand Falls basalt and (**b**) corresponding mineral phase map showing distribution of modeled plagioclase ("P" = medium gray), glass ("G" = light gray), and other mineral phases ("O" = dark gray); fields of view are 0.38 mm across. (**c**) BSE image of SP Flow basaltic andesite, and (**d**) mineral phase map showing zoned clinopyroxene crystals ("CPX"), with same grayscale key as in **b**; fields of view are 0.19 mm across.

Spectral deconvolutions

We used a combinatorial linear deconvolution model modified from the multiple end-member spectral mixing algorithm (MESMA) of Roberts et al. (1998) to deconvolve emission spectra of the unshocked and shocked basalts. Our implementation of the MESMA algorithm models an emissivity spectrum using a linear combination of specific end-members (e.g., Thompson and Salisbury 1993; Ramsey and Christensen 1998; Ramsey 2002; Bandfield 2002; Dennison et al. 2004) by solving for the best subset of mineral components from a larger reference library (e.g., Johnson et al. 2003; Staid et al. 2004). We selected 32 common minerals from the Arizona State University database (Christensen et al. 2000), and K-rich and silica-rich glasses from Wyatt et al. (2001) and Hamilton et al. (2001), respectively, to comprise our default end-member spectral library (Table 2a), identical to that used by Johnson et al. (2002). Additional models were run in which the end-member library was supplemented with the shocked and unshocked anorthosite chips from Johnson et al. (2002) and the shocked and unshocked albitite chips from Johnson et al. (2003) (Table 2b). The combinatorial deconvolution algorithm selected the best subset of components required to model the input spectrum through iterative comparisons to the spectral library to minimize uncertainties in the derived fractional abundances.

The algorithm initially compared all possible four-end-member combinations based on the spectral library components and a blackbody (Staid et al. 2001, 2004). The blackbody was used to compensate for grain size variations between the rock spectra and the library spectra (cf. Ramsey and Christensen 1998; Hamilton and Christensen 2000). The best model containing positive end-member abundances for each input spectrum was identified on the basis of the root-mean-square (rms)

Table 2a. End-member library used in MESMA deconvolutions (unshocked)

Andesine BUR-240	Bronzite BUR-1920	Forsterite BUR-3720A
Serpentine HS-8.4B	Muscovite WAR-5474	Oligoclase WAR-0234
Biotite BUR-840	Albite WAR-0612	Actinolite HS-116.4B
Enstatite HS-9.4B	Chlorite WAR-1924	Microcline BUR-3460
Hematite BUR-2600	Quartz BUR-4120	Labradorite WAR-4524
Augite BUR-620	Gypsum var. Alabaster ML-S11	Anhydrite ML-S9
Calcite ML-C9	Dolomite C17	Augite NMNH-119197
Diopside NMNH-R17421	Fayalite WAR-RGFAY01	Hornblende NMNH-R7208
Bytownite WAR-1384	Anorthite BUR-340	Kaolinite KGa-1b solid
Ca-montmorillonite STx-1 solid	Na-montmorillonite SWy-2 solid	Nontronite WAR-5108 granular
Fe-smectite SWa-1 granular	Hedenbergite NMNH-16168	K-rich glass
Silica-rich glass		

Note: All end-members acquired from Christensen et al. (2000), except for K-rich and silica-rich glasses, which were from Wyatt et al. (2001) and Hamilton et al. (2001), respectively.

error computed for each four-end-member combination. Then each unused library end-member was alternately added to the four end-members and a new rms error was calculated. The spectrum that provided the best improvement (and was selected with a positive abundance for all end-member components) was then kept as a fifth end-member. If no additional spectrum resulted in all positive fractions and an improved error, four end-members comprised the solution. This procedure was then repeated until as many as 12 end-members were selected. The algorithm produced fractions for each member chosen from the spectral library and a blackbody component. We ran the combinatorial demixing algorithm over the spectral range 400 to 1400 cm^{-1} with and without spectra of the shocked feldspars in the spectral library.

Results

BSE analyses

The main mineral classes and their modeled abundances for the Grand Falls basalt derived from the BSE images included plagioclase (48%), glass (11%), pyroxene (28%), and olivine (4%). Plagioclase and glass were distinguishable in chemical maps primarily via Al, Ca, K, and Si abundances. Aluminum and Ca correlate with plagioclase, whereas K is sequestered in the interstitial glass phase, and the Si content was significantly higher in the glass phase compared to plagioclase. Sodium correlated most strongly with plagioclase rims but also occurred in the glass. A second plagioclase ROI was defined to account for this composition. There was less distinction between Na-rich plagioclase and glass ROIs, and it is possible that some Na-rich plagioclase was misidentified as glass. The errors in Grand Falls plagioclase and glass content were estimated to be <5% within the region sampled in the BSE images.

The main mineral classes and their modeled abundances for SP Flow basaltic andesite were plagioclase (45%), glass (31%), pyroxene (18%), and olivine (<1%). Although plagioclase and glass were distinguished on a basis similar to the Grand Falls sample, the K in some SP Flow feldspars made plagioclase and glass less chemically distinguishable than in the Grand Falls sample. Further, the SP Flow sample was more difficult to analyze by this method because of its much finer grain size. In BSE images of the SP Flow sample, the glassy regions appeared less uniform, suggesting that they included more plagioclase microlites. As such, the glass content reported for SP Flow probably represents an upper limit. Given these characteristics, the errors associated with plagioclase and glass contents in the SP Flow sample were estimated to be ~8% within the region sampled in the BSE images.

Thermal infrared spectra

The spectra of the unshocked and shocked Grand Falls samples are shown in Figure 2. Unshocked spectra were acquired of both chips and the blocks from which the thin sections were made. Absorptions in the unshocked sample near 1100, 920, 520, and 400 cm^{-1} result from Si-O vibrations in dominantly Ca-rich plagioclase feldspars with some contributions from pyroxene and olivine. With increasing pressure, the progressive structural disorder caused the Si-O absorption bands in feldspars to shift and merge such that the highest shock pressures resulted in spectra with absorptions broadly centered near 960 and 400 cm^{-1}. As a result of the two principal long-wavenumber bands merging, the Christiansen Feature (CF; the maximum emissivity in the 1200

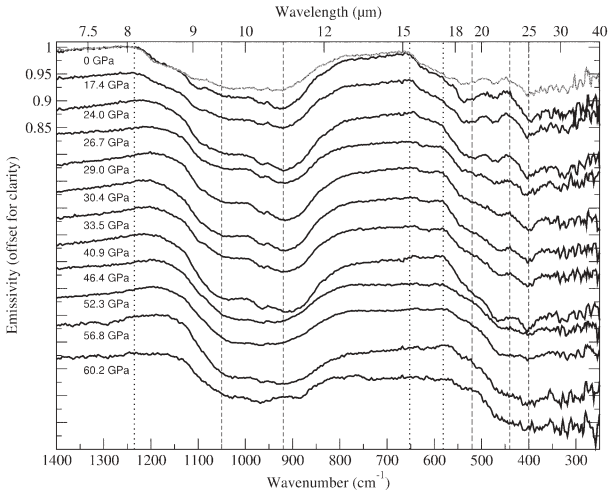

Figure 2. Emissivity spectra of Grand Falls basalt chips recovered from shock experiments, with shock pressures labeled below each spectrum. Two spectra for unshocked samples (0 GPa) are overlain: The chips spectrum is shown in gray (top light), and the block from which thin sections were made is shown in black. All shocked spectra are offset from the unshocked spectra. Vertical lines represent spectral regions of interest at 1235, 1050, 920, 652, 581, 520, 440, and 400 cm^{-1}.

Table 2b. End-member library of shocked and unshocked feldspars used in MESMA deconvolutions

Anorthosite (GPa)	Albitite (GPa)
0	0
17.0	17.0
21.0	24.0
21.5	25.5
22.6	27.8
25.5	29.0
27.0	31.4
37.5	34.8
38.2	38.0
49.2	44.6
56.3	50.0
	55.8

Note: Anorthosite data from Johnson et al. (2002); Albitite data from Johnson et al. (2003).

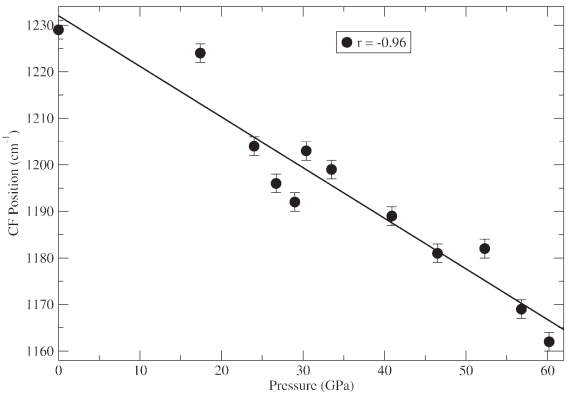

FIGURE 3. Variation of Christiansen Feature (CF) position with pressure for Grand Falls basalt samples. Linear fit and correlation coefficient (*r*) shown. Error bars represent 2 cm^{-1} spectral sampling of measurements.

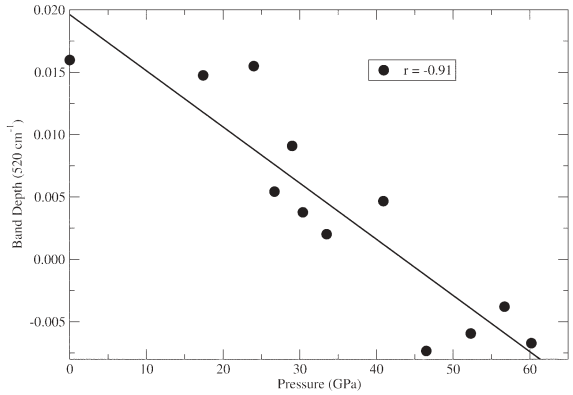

FIGURE 4. Increase of 520 cm^{-1} band depth with pressure for Grand Falls basalt samples. Linear fit and correlation coefficient (*r*) shown.

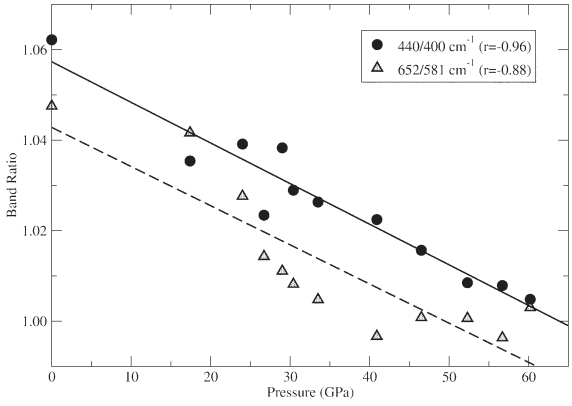

FIGURE 5. Decrease in 440/400 cm^{-1} and 652/581 cm^{-1} ratios as a function of shock pressure in the Grand Falls samples, with linear fits and correlation coefficients shown.

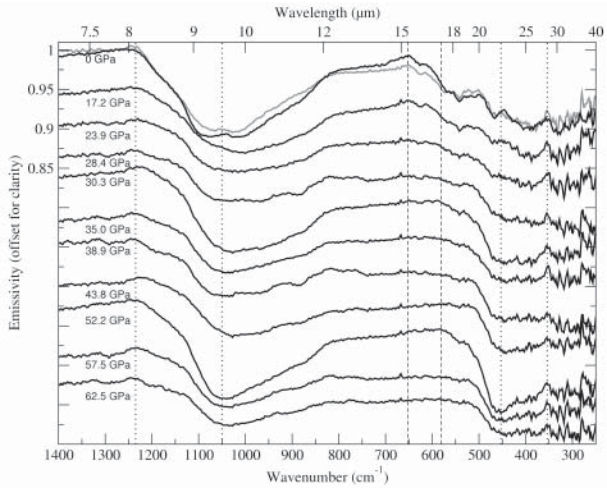

FIGURE 6. Emissivity spectra of SP Flow basaltic andesite chips recovered from shock experiments, with shock pressures labeled below each spectrum. Two spectra for unshocked samples (0 GPa) are overlain: The chips spectrum is shown in gray, and the block from which thin sections were made is shown in black. The contrast of the block spectrum has been reduced by 25% to better fit on the plot. All spectra are offset from the unshocked spectra. Vertical lines represent spectral regions of interest at (left to right) 1235, 1050, 652, 581, 453, and 354 cm^{-1}.

cm^{-1} region) shifted to smaller wavenumbers with increasing pressure, as shown in Figure 3. At shorter wavenumbers other absorption bands disappeared, and the spectral slopes related to such bands flattened. For example, the 520 cm^{-1} band depth for each pressure (Fig. 4) was calculated by computing [1 – (ε_{520}/*continuum*)] where ε_{520} is the emissivity value at 520 cm^{-1}, and the *continuum* was computed between bands at 559 and 484 cm^{-1} (cf. Clark and Roush 1984; Bell and Crisp 1993). In Figure 5, the 440/400 cm^{-1} ratio is highly negatively correlated with increasing shock pressures owing to the loss of the narrow 400 cm^{-1} band and the 440 cm^{-1} local emissivity maximum. The 652/581 cm^{-1} ratio is less well correlated with pressure, although the initially steep spectral slope in this region related to the 535 cm^{-1} band was minimized by 35–40 GPa (Fig. 5).

The SP Flow basaltic andesite spectra are shown in Figure 6, where a broader absorption centered near 1050 cm^{-1} in the unshocked sample is characteristic of basaltic andesite (e.g., Bandfield et al. 2000), and the relative lack of prominent spectral features in the <500 cm^{-1} region is attributable to the lower abundances of olivine and pyroxene relative to primary glass content. Spectra acquired at higher pressures mainly exhibited the development of a band centered near 450 cm^{-1}. Figure 7 shows how the 652/581 cm^{-1} ratio decreases with increasing pressure and the gradual loss of crystal structure, as does the 453/354 cm^{-1} ratio. The band near 1050 cm^{-1} and the CF near 1235 cm^{-1} changed little in position from the unshocked spectra. The differences in spectral contrast among the data evident in Figure 6 likely resulted from subtle variations in the amount of sample available to fill the ~1 cm field of view of the spectrometer.

Spectral deconvolutions

Table 3 compares the mineral abundances calculated from the BSE analyses for each sample type to those from the spectral deconvolutions for the unshocked chips and blocks. The plagio-

clase contents of both samples derived from the BSE method are 5–10% lower than the spectral deconvolution abundances. This difference may result from the presence of plagioclase microlites (and/or crystalline domains in the mesostasis) to which infrared spectroscopy is more sensitive than the BSE technique (P. Christensen, pers. comm.). The BSE-derived pyroxene and glass contents are consistently higher than the deconvolution results, although typically within the 5–15% uncertainties associated with deconvolution models (e.g., Feely and Christensen 1999). The overestimation of glass contents by the BSE technique may be a consequence of the similarity in chemistry between the glass and plagioclases, as discussed above. If the ~10% excess glass abundances were distributed among the plagioclase and "Other" category, the BSE and deconvolution abundances in Table 3 would balance better. Olivine abundances for the SP Flow samples are consistently very low, whereas those derived for the Grand Falls basalt vary between 4 and 15%. The higher abundance in the chips sample may simply reflect the presence of additional olivine phenocrysts that were absent in the block sample. Similarly, variations in pyroxene phenocrysts between the Grand Falls chips and block samples may explain their variations in Table 3.

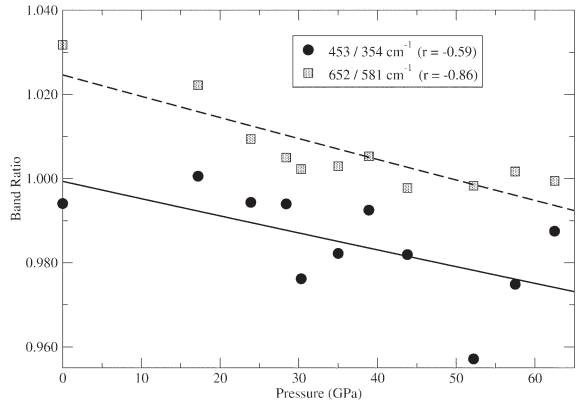

FIGURE 7. Decrease in 453/354 and 652/581 cm^{-1} ratios as a function of shock pressure in the SP Flow samples, with linear fits and correlation coefficients shown.

Figure 8 shows a comparison of four representative shocked Grand Falls basalt spectra and model results from the deconvolutions in which shocked anorthosite and albitite feldspars were absent (Fig. 8a) and included (Fig. 8b) in the end-member library. These results demonstrate an improvement in rms error and visual fit quality when shocked feldspars were included in the spectral library. The number of end-members selected for the deconvolutions using the shocked feldspars was less than or equal to the number used for the deconvolutions without the shocked feldspars, further indicating that inclusion of the shocked feldspars provides an overall better fit. A similar result was found for the SP Flow basaltic andesite data in Figure 9, where inclusion of the shocked feldspars improved the rms error and overall fit quality, and decreased the number of required end-members for all but the 57.5 GPa case. Although the deconvolution results potentially could be improved further by experimenting with additional minerals in the spectral library, the main conclusion that the shocked feldspars improved the overall fits is clear.

Figure 10 further illustrates this point by comparing the variation in model rms error with pressure for both Grand Falls and SP Flow data sets when deconvolutions were run with and without shocked feldspars. The improvement in rms error for deconvolu-

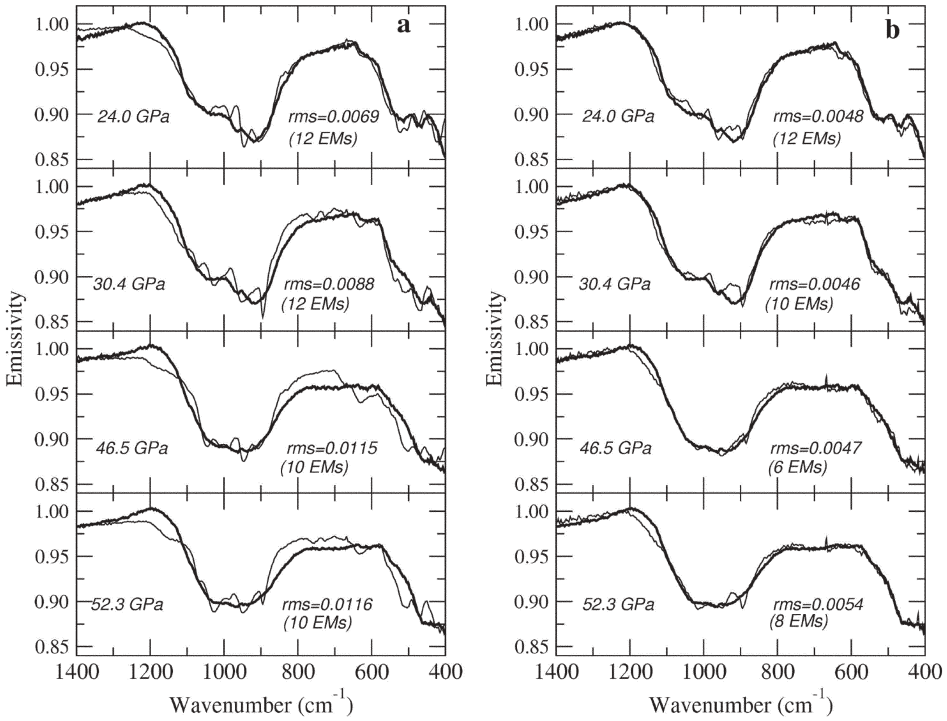

FIGURE 8. Comparison of measured (thick line) and deconvolved (modeled; thin line) spectra of Grand Falls shocked chips (24.0, 30.4, 46.5, 52.3 GPa) using a spectral library that withheld shocked feldspars (**a**) and a library that contained shocked feldspars (**b**). Deconvolution rms errors shown along with number of selected end-members (EMs) from the deconvolution run. Note decrease in rms error using shocked feldspars end-members, as well as general decrease in number of end-members selected by fit.

TABLE 3. Mineral group abundances (areal percent) calculated from BSE analyses and spectral deconvolutions of unshocked Grand Falls and SP Flow basalts

	Grand Falls (BSE)	Grand Falls (spectral: chips)	Grand Falls (spectral: block)	SP Flow (BSE)	SP Flow (spectral: chips)	SP Flow (spectral:block)
Plagioclase	47.8	56.0	55.6	44.5	49.0	47.7
Pyroxene	27.8	6.5	16.6	17.8	4.3	6.6
Olivine	4.0	15.1	8.2	0.3	1.6	0.0
Glass	11.1	0.0	1.9	30.7	19.0	20.1
Other*	9.3	23.7	17.7	6.7	26.1	25.6

* "Other" includes sheet silicates, carbonates, Fe-oxides, and apatite.

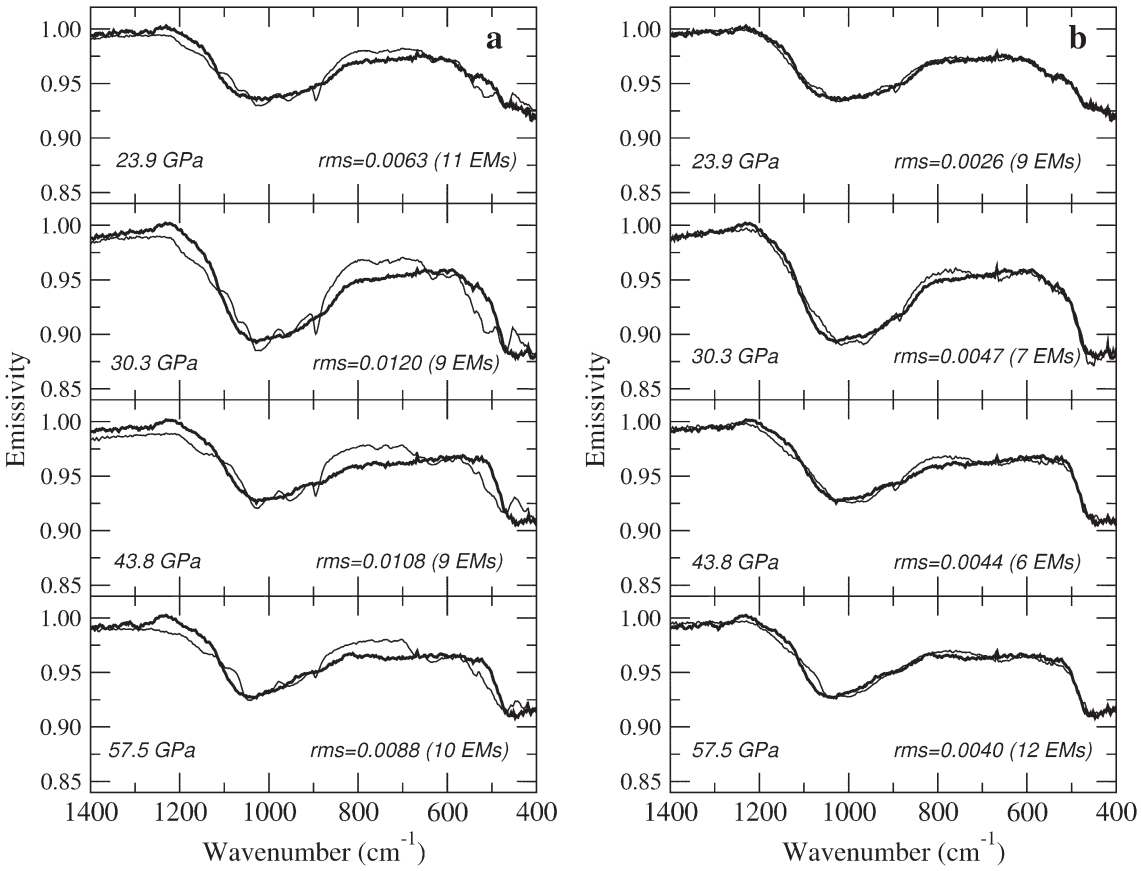

FIGURE 9. Comparison of measured (thick line) and deconvolved (modeled; thin line) spectra of SP Flow shocked chips (23.9, 30.3, 43.8, 57.5 GPa) using a spectral library that withheld shocked feldspars (**a**) and a library that contained shocked feldspars (**b**). Deconvolution rms errors shown along with number of selected end-members (EMs) from deconvolution run. Note decrease in rms error using shocked feldspars end-members, as well as general decrease in number of end-members selected by fit.

tions that included shocked feldspars is evident in both samples. In the Grand Falls data (Fig. 10a), the improvement in rms errors increased substantially at pressures >17 GPa, consistent with the onset of diaplectic glass formation that is much better modeled by inclusion of the shocked feldspars. Conversely, the SP Flow data (Fig. 10b) showed a more constant difference in rms errors with pressure. This may result from the greater proportion of primary glass content in these samples compared to the Grand Falls rocks. To investigate this further, we calculated the modeled shock pressure value from each deconvolution by scaling the pressure of each selected shocked feldspar by its modeled abundance and summing the results. Figure 11 compares the measured and averaged modeled pressures for the two basaltic samples. For the Grand Falls data, the unshocked sample was modeled with low shock pressures as expected, and the data were relatively accurate until a plateau was reached at measured shock pressures >30 GPa. We interpret the observed trend to reflect the onset of diaplectic glass formation between 20 and 25 GPa. At higher pressures, the increasing amount of diaplectic glass disproportionately biases the modeled shock pressures to inappropriately large values until about 45 GPa. In this pressure range, nearly complete melting of the feldspar occurs and the model more accurately reports the measured shock pressure of the basalt. The fall-off of this trend at the highest shock pressures

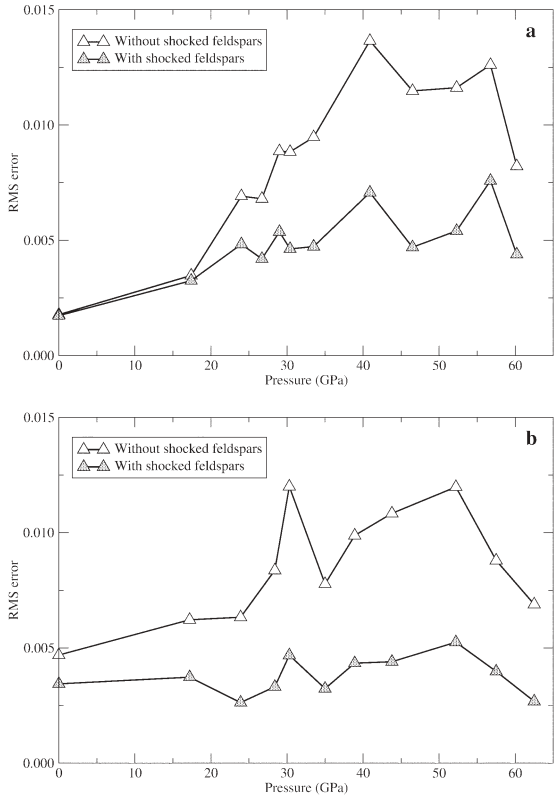

FIGURE 10. RMS error variations as a function of shock pressure for (**a**) Grand Falls and (**b**) SP Flow samples for deconvolutions in which shocked feldspars were included and withheld from spectral libraries. Both sample sets exhibit lower rms errors when shocked feldspars are included. The divergence in rms error trends after 17 GPa for the primary glass-poor Grand Falls samples is indicative of the onset of glass formation in more highly shocked samples. The lack of such divergence in the SP Flow samples indicates the effects of primary glass.

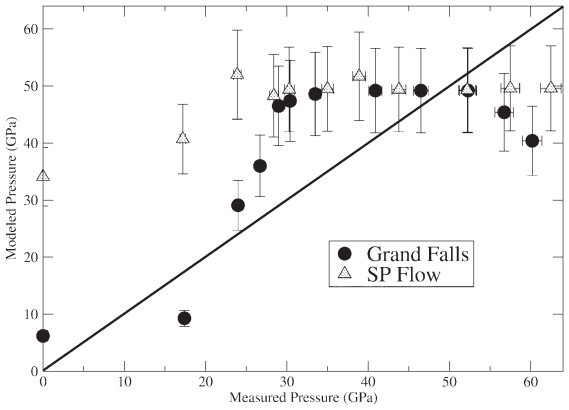

FIGURE 11. Measured and average modeled shock pressures for Grand Falls and SP Flow samples. Grand Falls samples exhibit an upturn in modeled pressures after 17 GPa, followed by a relatively constant modeled pressure (~47 GPa) after 30 GPa measured pressure and a slight downturn >50 GPa measured pressure. The SP Flow samples show high pressures even for the unshocked sample, followed by a nearly constant modeled pressure similar to the >30 GPa Grand Falls sample results. Solid line is 1:1 correlation. Error bars represent 15% uncertainties on modeled pressures and 2% error on measured pressures.

(>50 GPa) may result from the relatively low spectral contrast of these samples owing to their small retrieved volume from the shock experiments and subsequent inability to completely fill the field of view of the spectrometer.

For the SP Flow sample, the model incorrectly predicted a high shock pressure for the unshocked sample. This was followed by a small increase in modeled pressure until a similar plateau was reached near 25–30 GPa, after which the modeled pressures were consistently ~50 GPa. We interpret this trend to reflect the higher primary glass content of the SP Flow samples, which confuses the model even at 0 GPa shock pressure because of the apparent spectral similarity between highly shocked feldspars and volcanic glass. The two dominant end-members selected for the unshocked SP Flow sample from deconvolutions run without the shocked feldspars were bytownite (47%) and K-rich glass (18%). When the shocked feldspars were added to the library, the same sample was modeled to contain bytownite (5%), mildly shocked anorthosite feldspars (16% of 22.6 GPa, and 8% of 25.5 GPa), and a large amount of highly shocked albitite (39% of 44.6 GPa). Indeed, one common theme among the SP Flow deconvolutions that included shocked feldspars was the selection of shocked albitite in every model except the 23.9 GPa sample. For comparison, the only shocked Grand Falls sample to be modeled with any shocked albitite was the 24.0 GPa sample. The preference for albitite likely occurs because the SP Flow and albitite spectra exhibit similar long-wavenumber bands in the 1000–1200 cm^{-1} region. The Grand Falls and anorthosite spectra share similar, shorter-wavenumber bands in this region (e.g., Johnson et al. 2003). Furthermore, the position of the main long-wavenumber absorptions in highly shocked feldspars vary from ~950 cm^{-1} in bytownite to ~1050 cm^{-1} in albite (near the main band in the highly shocked SP Flow sample). Combined with the characteristic of albite to maintain its structural integrity (and infrared spectral features) to higher shock pressures than anorthite (Williams 1998; Johnson et al. 2003; Milyavskiy et al. 2006), the overestimation of shock pressures in the SP Flow samples may be abetted by the models' selections of shocked albitites.

CONCLUDING REMARKS

The experimentally shocked basalt and basaltic andesite presented here exhibit thermal infrared spectral absorptions that degrade, shift, and/or merge with increasing pressure. These distinctive spectral changes are caused by pressure-induced structural distortions in the bending and stretching motions of Si and Al tetrahedra dominantly within plagioclase feldspars (e.g., Ostertag 1983; Johnson et al. 2002, 2003). As shock pressures increase, spectral features vary in a relatively linear fashion and result in broad bands near 960 and 400 cm^{-1}. Similar types of absorptions are observed in some glasses (e.g., Wyatt et al. 2001; Byrnes et al. 2007), silica coatings (Kraft et al. 2003; Michalski et al. 2005), clay minerals (Michalski et al. 2006), altered/oxidized basalts (Minitti et al. 2002; Hamilton and Minitti 2003),

and zeolites (Ruff 2004).

Spectral deconvolution models of the unshocked rock spectra provided abundances of plagioclase and glass that were consistent with the values determined from supervised classification models run on BSE images. However, deconvolution models run for shocked samples using the same mineral reference libraries resulted in poorer overall fits, particularly at high shock pressures. By adding shocked feldspars to the end-member libraries (Johnson et al. 2002, 2003), the deconvolution model fits improved both quantitatively and qualitatively. In particular, the Grand Falls basalt samples exhibited improved rms errors beginning at shock pressures ~20–25 GPa at which the onset of diaplectic glass formation occurs in plagioclase. For these samples, modeled shock pressures were accurate to ±10 GPa except between ~28 and 40 GPa, where the model overestimated the measured shock pressures. Although the SP Flow basaltic andesite exhibited similar improvements in model fits upon inclusion of shocked feldspars in the end-member library, shocked feldspars were incorrectly selected by models of unshocked sample spectra. This result suggests that the higher primary glass content of the basaltic andesite samples (20–30%) confused the deconvolution algorithm. Indeed, all modeled pressures were overestimated for the SP Flow samples until ~40 GPa, after which values accurate to ±10 GPa were modeled.

The shocked samples studied here are large chips, which have significant spectral differences compared to their powdered counterparts (e.g., Johnson et al. 2002, 2003). As such, the data presented here are more relevant for comparison to rocky, large-grained surfaces than to the fine-grained regoliths that dominate large portions of the Moon, Mercury, and asteroids. However, because linear mixture models of fine-grained materials are inappropriate owing to the non-linear effects of volume scattering (e.g., Ramsey and Christensen 1998), the large chip samples provide the most direct means to study the spectral effects of shock pressures from remotely sensed planetary data, particularly for Mars and Earth. Indeed, the results presented here suggest that incorporating spectra of shocked feldspars or basaltic rocks as end-members for deconvolutions of remotely sensed data may provide useful information regarding the shock state of the surfaces analyzed (e.g., Tornabene et al. 2005; Johnson et al. 2006). However, the first-order similarity in spectral absorptions among primary volcanic glass and other crystalline or amorphous/glassy compositions could lead to spurious interpretations of the inferred shock pressures. Additional laboratory studies are needed to better distinguish among volcanic glass, impact-generated glasses, and other poorly crystalline or amorphous materials such as coatings. Further experimental work on the shock-induced spectral changes observed for intermediate composition plagioclase feldspars (e.g., labradorite) should provide additional constraints on interpreting the effects of shock on planetary bodies.

Acknowledgments

This work was supported by the Planetary Geology and Geophysics Program. We thank J. Plescia (APL) for assistance with sample collection, F. Hörz (JSC) for overseeing the shock experiments and for his interest in this work, as well as support from P. Christensen and the ASU Thermal Emission Spectroscopy Laboratory and M. Minitti and the Center for Meteorite Studies. We also thank J. Byrnes and L. Keszthelyi (USGS) for helpful preliminary reviews of the manuscript, and A. Sprague and C. Dufresne for formal reviews.

References cited

Arndt, J., Hummel, W., and Gonzalez-Cabeza, I. (1982) Diaplectic labradorite glass from the Manicouagan impact crater, I. Physical properties, crystallization, structural and genetic implications. Physics and Chemistry of Minerals, 8, 230–239.

Bandfield, J.L. (2002) Global mineral distributions on Mars. Journal of Geophysical Research, 107(E6), 5042, DOI: 10.1029/2001JE001510.

Bandfield, J.L., Hamilton, V.E., and Christensen, P.R. (2000) A global view of Martian surface compositions from MGS-TES. Science, 287, 1626–1630.

Bell, J.F., III and Crisp, D. (1993) Groundbased imaging spectroscopy of Mars in the near-infrared—Preliminary results. Icarus, 104, 2–19.

Bunch, T.E., Cohen, A.J., and Dence, M.R. (1967) Natural terrestrial maskelynite. American Mineralogist, 52, 244–253.

——— (1968) Shock-induced structural disorder in plagioclase and quartz. In Shock Metamorphism of Natural Materials, Proceedings of the First Conference, Mono Book Corp., Baltimore, 509–518.

Byrnes, J.M., Ramsey, M.S., King, P.L., and Lee, R.J. (2007) Thermal infrared reflectance and emission spectroscopy of quartzofeldspathic glasses. Geophysical Research Letters, 34, L01306, DOI: 10.1029/2006GL027893.

Christensen, P.R., Anderson, D.L., Chase, S.C., Clancy, R.T., Clark, R.N., Conrath, B.J., Kieffer, H.H., Kuzmin, R.O., Malin, M.C., Pearl, J.C., Roush, T.L., and Smith, M.D. (1998) Results from the Mars global surveyor thermal emission spectrometer. Science, 279, 1692–1698.

Christensen, P.R., Bandfield, J.L., Hamilton, V.E., Howard, D.A., Lane, M.D., Piatek, J.L., Ruff, S.W., and Stevanov, W.L. (2000) A thermal emission spectral library of rock-forming minerals. Journal of Geophysical Research, 105, 9735–9739.

Christensen, P.R., Bandfield, J.L., Hamilton, V.E., Ruff, S.W., Kieffer, H.H., Titus, T.N., Malin, M.C., Morris, R.V., Lane, M.D., Clark, R.L., Jakosky, B.M., Mellon, M.T., Pearl, J.C., Conrath, B.J., Smith, M.D., Clancy, R.T., Kuzmin, R.O., Roush, T., Mehall, G.L., Gorelick, N., Bender, K., Murray, K., Dason, S., Greene, E., Silverman, S., and Greenfield, M. (2001) The Mars global surveyor thermal emission spectrometer experiment: Investigation description and surface science results. Journal of Geophysical Research, 106, 23823–23871.

Clark, R.N. and Roush, T.L. (1984) Reflectance spectroscopy—Quantitative analysis techniques for remote sensing applications. Journal of Geophysical Research, 89, 6329–6340.

Cooney, T.F., Scott, E.R.D., Krot, A.N., Sharma, S.K., and Yamaguchi, A. (1999) Vibrational spectroscopic study of minerals in the Martian meteorite ALH84001. American Mineralogist, 84, 1569–1576.

Daniel, I., Gillet, P., and Ghose, S. (1995) A new high-pressure phase transition in anorthite ($CaAl_2Si_2O_8$) revealed by Raman spectroscopy. American Mineralogist, 80, 645–648.

Daniel, I., Gillet, P., McMillan, P.F., Wolf, G., and Verhelst, M.A. (1997) High-pressure behavior of anorthite: Compression and amorphization. Journal of Geophysical Research, 102, 10313–10325.

DeCarli, P.S., Bowden, E., Jones, A.P., and Price, G.D. (2002) Laboratory impact experiments versus natural impact events. In C. Koeberl and K.G. MacLeod, Eds., Catastrophic events and mass extinctions: Impacts and beyond: Boulder, Colorado. Geological Society of America Special Paper 356, 595–605.

Dennison, P.E., Halligan, K.Q., and Roberts, D.A. (2004) A comparison of error metrics and constraints for multiple end-member spectral mixture analysis and spectral angle mapper. Remote Sensing of Environment, 93, 359–367.

Feely, K.C. and Christensen, P.R. (1999) Quantitative compositional analysis using thermal emission spectroscopy: Application to igneous and metamorphic rocks. Journal of Geophysical Research, 104, 24195–24210.

Fritz, J., Greshake, A., Hecht, L., and Stöffler, D. (2002) Shock metamorphism of Martain meteorites: New data from quantitative shock barometry. Lunar and Planetary Science Conference XXXIII, Abstract no. 1504.

Gibbons, R.V., Morris, R.V., Hörz, F., and Thompson, T.D. (1975) Petrographic and ferromagnetic resonance studies of experimentally shocked regolith analogs. In Proceedings of the 6th Lunar Science Conference, Houston, 3, p. 3143–3171. Pergamon Press, New York.

Hamilton, V.E. and Christensen, P.R. (2000) Determining the modal mineralogy of mafic and ultramafic igneous rocks using thermal emission spectroscopy. Journal of Geophysical Research, 105, 9717–9733.

Hamilton, V.E. and Minitti, M.E. (2003) Are oxidized shergottite-like basalts an alternative to "andesite" on Mars? Geophysical Research Letters, 30, 1915, DOI: 10.1029/2003GL017839.

Hamilton, V.E., Wyatt, M.B., McSween, H.Y., and Christensen, P.R. (2001) Analysis of terrestrial and Martian volcanic compositions using thermal emission spectroscopy: 2. Application to Martian surface spectra from the Mars global surveyor thermal emission spectrometer. Journal of Geophysical Research, 106, 14733–14746.

Heymann, D. and Hörz, F. (1990) Raman-spectroscopy and X-ray diffractometer studies of experimentally produced diaplectic feldspar glass. Physics and Chemistry of Minerals, 17, 38–44.

Hörz, F. and Cintala, M. (1997) Impact experiments related to the evolution of planetary regoliths. Meteoritics and Planetary Science, 32, 179–209.

Iiishi, K., Tomisaka, T., Kato, T., and Umegaki, Y. (1971) Isomorphous substitution and infrared and far infrared spectra of the feldspar group. Neues Jahrbuch fuer Mineralogie. Abhandlungen, 115, 98–119.

Johnson, J.R., Hörz, F., Christensen, P., and Lucey, P.G. (2002) Thermal infrared spectroscopy of experimentally shocked anorthosite and pyroxenite: Implications for remote sensing of Mars. Journal of Geophysical Research, 107(E10), 5073, DOI: 10.1029/2001JE001517.

Johnson, J.R., Hörz, F., and Staid, M.I. (2003) Thermal infrared spectroscopy and modeling of experimentally shocked plagioclase feldspars. American Mineralogist, 88, 1575–1582.

Johnson, J.R., Staid, M.I., Titus, T.N., and Becker, K. (2006) Shocked plagioclase signatures in Thermal Emission Spectrometer data of Mars. Icarus, 180, 60–74.

Jones, A.H., Isbell, W.M., and Maiden, J.C. (1966) Measurements of the very-high-pressure properties of materials using a light-gas gun. Journal of Applied Physics, 37, 3493–3499.

King, P.L., McMilland, P.F., and Moore, G.M. (2004) Chapter 4. Infrared spectroscopy of silicate glasses with application to natural systems. In P.L. King, M.S. Ramsey, and G.A. Swayze, Eds., Infrared spectroscopy in geochemistry, exploration geochemistry and remote sensing. Mineralogical Association of Canada, Short Course 33, 93–133.

Kraft, M.D., Michalski, J.R., and Sharp, T.G. (2003) Effects of pure silica coatings on thermal emission spectra of basaltic rocks: Considerations for Martian surface mineralogy. Geophysical Research Letters, 30, 2288, DOI: 10.1029/2003GL018848.

Lyon, R.J.P. (1963) Evaluation of infrared spectrophotometry for compositional analysis of lunar and planetary soils. NASA Technical Note D-1871.

Marsh, S.P. (1980) LASL Shock Hugoniot Data, 658 p. University of California Press, Berkeley.

Michalski, J.R., Kraft, M.D., Sharp, T.G., Williams, L.B., and Christensen, P.R. (2005) Mineralogical constraints on the high-silica martian surface component observed by TES. Icarus, 174, 161–177.

——— (2006) Emission spectroscopy of clay minerals and evidence for poorly crystalline aluminosilicates on Mars from Thermal Emission Spectrometer data. Journal of Geophysical Research, 111, E03004, DOI: 10.1029/2005JE002438.

Milyavskiy, V.V., Sazonova, L.V., Borodina, T.I., Sokolov, S.N., Beljatinskaja, I.V., and Zhernokletov, D.M. (2006) Plagioclase and amphibole transformations in conditions of step-like shock compression of crystal schist. Lunar and Planetary Science Conference XXXVII, abstract no. 1076.

Minitti, M.E., Mustard, J.F., and Rutherford, M.J. (2002) Effects of glass content and oxidation on the spectra of SNC-like basalts: Applications to Mars remote sensing. Journal of Geophysical Research, 107(E5), DOI: 10.1029/2001JE001518.

Morris, P.W., Heras, A.M., Vandenbussche, B., and Dijkstra, R. (1999) Asteriod 4 Vesta as seen with the infrared space observatory short wavelength spectrometer. LPI Contribution, Report 969, 19–20.

Ostertag, R. (1983) Shock experiments on feldspar crystals, Proceedings of the 14th Lunar Planetary Science Conference, Journal of Geophysical Research, 88, B364–B376.

Palomba, E., Rotundi, A., and Colangeli, L. (2006) Infrared micro-spectroscopy of the martian meteorite Zagami: Extraction of individual mineral phase spectra. Icarus, 182, 68–79.

Ramsey, M.S. (2002) Ejecta distribution patterns at Meteor Crater, Arizona: On the applicability of lithologic end-member deconvolution for spaceborne thermal infrared data of Earth and Mars. Journal of Geophysical Research, 107(E8), DOI: 10.1029/2001JE001827.

Ramsey, M.S. and Christensen, P.R. (1998) Mineral abundance determination: Quantitative deconvolution of thermal emission spectra. Journal of Geophysical Research, 103, 577–596.

Roberts, D.A., Gardner, M., Church, R., Ustin, S., Sheer, G., and Green, R.O. (1998) Mapping Chaparral in the Santa Monica mountains using multiple end-member spectral mixture models. Remote Sensing of Environment, 65, 267–269.

Ruff, S.W. (2004) Spectral evidence for zeolite in the dust of Mars. Icarus, 168, 131–143.

Ruff, S.W., Christensen, P.R., Barbera, P.W., and Anderson, D.L. (1997) Quantitative thermal emission spectroscopy of minerals: A technique for measurement and collection. Journal of Geophysical Research, 102, 14899–14913.

Salisbury, J.W., Murcray, D.G., Williams, W.J., and Blatherwick, R.D. (1995) Thermal infrared spectra of the Moon. Icarus, 115, 181–190.

Salisbury, J.W., Basu, A., and Fischer, E.M. (1997) Thermal infrared spectra of lunar soils. Icarus, 130, 125–139.

Sprague, A.L., Emery, J.P., Donaldson, K.L., Russell, R.W., Lynch, D.K., and Mazuk, A.L. (2002) Mercury: Mid-infrared (3–13.5 μm) observations show heterogeneous composition, presence of intermediate and basic soil types, and pyroxene. Meteoritics and Planetary Science, 37, 1255–1268.

Staid, M.I., Gaddis, L.R., and Titus, T. (2001) A new approach for mapping minerals on Mars with TES data, EOS. Transactions of the American Geophysical Union (abstract), P42A-0553.

Staid, M.I, Johnson, J.R., and Gaddis, L.R. (2004) Analysis of Mars Thermal Emission Spectrometer data using large mineral reference libraries. Lunar and Planetary Science Conference XXXV, abstract no. 1778.

Stöffler, D. (1971) Progressive metamorphism and classification of shocked and brecciated crystalline rocks at impact craters. Journal of Geophysical Research, 76, 5541–5551.

——— (1972) Deformation and transformation of rock-forming mineral by natural and experimental shock processes I. Behavior of minerals under shock compression. Fortschrite Mineralogie, 49, 50–113.

——— (1974) Deformation and transformation of rock-forming minerals by natural and experimental shock processes, II. Physical properties of shocked minerals. Fortschrite Mineralogie, 51, 256–289.

——— (2001) Maskelynite confirmed as diaplectic glass: Indication for peak shock pressures below 45 GPa in all Martian meteorites. Lunar and Planetary Science Conference XXXII, abstract no. 1170.

Stöffler, D. and Hornemann, U. (1972) Quartz and feldspar glasses produced by natural and experimental shock. Meteoritics, 7, 371–394.

Thoma, K., Hornemann, U., Sauer, M., and Schneider, E. (2005) Shock waves—Phenomenology, experimental, and numerical simulation. Meteoritics and Planetary Science, 40, 1283–1298.

Thompson, J. and Salisbury, J. (1993) The mid-infrared reflectance of mineral mixtures (7–14 μm). Remote Sensing of Environment, 45, 1–13.

Tornabene, L.L., Moersch, J.E., Osinski, G.R., Lee, P., and Wright, S.P. (2005) Spaceborne visible and thermal infrared lithologic mapping of impact-exposed subsurface lithologies at the Haughton impact structure, Devon Island, Canadian High Arctic: Applications to Mars. Meteoritics and Planetary Science, 40, 1835–1858.

Ulrich, G.E. (1987) SP Mountain cinder cone and lava flow, northern Arizona. Rocky Mountain section Geological Society of America, Centennial field guide, 2, 385–388.

Velde, B., Syono, Y., Couty, R., and Kikuchi, M. (1987) High pressure infrared spectra of diaplectic anorthite glass. Physics and Chemistry of Minerals, 14, 345–349.

Velde, B., Syono, Y., Kikuchi, M., and Boyer, H. (1989) Raman microprobe study of synthetic diaplectic plagioclase feldspars. Physics and Chemistry of Minerals, 16, 436–441.

Williams, Q. (1998) High-pressure infrared spectra of feldspars: Constraints on compressional behavior, amorphization, and diaplectic glass formation. In M.H. Manghnani and T. Yagi, Eds., Properties of Earth and Planetary Materials at High Pressure and Temperature, p. 531–543. Geophysical Monograph 101, American Geophysical Union, Washington, D.C.

Williams, Q. and Jeanloz, R. (1988) Spectroscopic evidence for pressure-induced coordination changes in silicate glasses and melts. Science, 239, 902–905.

——— (1989) Static amorphization of anorthite at 300 K and comparison with diaplectic glass. Nature, 338, 413–415.

Wright, S.P., Johnson, J.R., and Christensen, P.R. (2004) Thermal emission spectra of impact glass and shocked Deccan basalt from Lonar crater, India and implications for remote sensing of Mars. Lunar and Planetary Science Conference XXXV, abstract no. 2072.

Wright, S.P., Christensen, P.R., and Sharp, T.G. (2006) Thermal emission spectroscopy of shocked basalt from the Earth and Mars: A review plus new insights. Lunar and Planetary Science Conference XXXVII, abstract no. 1786.

Wyatt, M.B., Hamilton, V.E., McSween, H.Y., Jr., Christensen, P.R., and Taylor, L.A. (2001) Analysis of terrestrial and Martian volcanic compositions using thermal emission spectroscopy: 1. Determination of mineralogy, chemistry, and classification strategies. Journal of Geophysical Research, 106, 14711–14732.

Xie, X., Chen, M., Dai, C., El Goresy, A., and Gillet, P. (2001) A comparative study of naturally and experimentally shocked chondrites. Earth and Planetary Science Letters, 187, 345–356.

Yamaguchi, A. and Sekine, T. (2000) Monomineralic mobilization of plagioclase by shock: an experimental study. Earth and Planetary Science Letters, 175, 289–296.

Manuscript received June 21, 2006
Manuscript accepted February 25, 2007
Manuscript handled by Rhian Jones